Ultrafast active control of localized surface plasmon resonances in silicon bowtie antennas

Audrey Berrier,[1,*] Ronald Ulbricht,[2] Mischa Bonn,[2] and Jaime Gómez Rivas[1]

[1]*FOM Institute AMOLF Centre for Nanophotonics c/o Philips Research Laboratories,HTC4, 5656AE Eindhoven, The Netherlands*
[2]*FOM Institute AMOLF Science Park 104, 1098XG Amsterdam, The Netherlands*
*a.berrier@amolf.nl

Abstract: Localized surface plasmon polaritons (LSPPs) provide an efficient means of achieving extreme light concentration. In recent years, their active control has become a major aspiration of plasmonic research. Here, we demonstrate direct control of semiconductor bowtie antennas, enabling active excitation of LSPPs, at terahertz (THz) frequencies. We modify the LSPPs by ultrafast optical modulation of the free carrier density in the plasmonic structure itself, allowing for active control of the semiconductor antennas on picosecond timescales. Moreover, this control enables the manipulation of the field intensity enhancements in ranges of four orders of magnitude.

©2010 Optical Society of America

OCIS codes: (240.6680) Surface Plasmons; (300.6495) Spectroscopy, Terahertz ; (250.6715) Switching ; (250.5403) Plasmonics ; (320.7130) Ultrafast processes including semiconductors ; (130.4815) Optical switching.

References and links

1. D. K. Gramotnev, and S. I. Bozhevolnyi, "Plasmonics beyond the diffraction limit," Nat. Photonics **4**(2), 83–91 (2010).
2. P. Mühlschlegel, H.-J. Eisler, O. J. F. Martin, B. Hecht, and D. W. Pohl, "Resonant optical antennas," Science **308**(5728), 1607–1609 (2005).
3. J. A. Schuller, E. S. Barnard, W. Cai, Y. C. Jun, J. S. White, and M. L. Brongersma, "Plasmonics for extreme light concentration and manipulation," Nat. Mater. **9**(3), 193–204 (2010).
4. S. Palomba, M. Danckwerts, and L. Novotny, "Nonlinear plasmonics with gold nanoparticle antennas," J. Opt. A, Pure Appl. Opt. **11**(11), 114030 (2009).
5. K. F. MacDonald, Z. L. Samson, M. I. Stockman, and N. I. Zheludev, "Ultrafast active plasmonics," Nat. Photonics **3**(1), 55–58 (2009).
6. H.-T. Chen, J. F. O'Hara, A. K. Azad, A. J. Taylor, R. D. Averitt, D. B. Shrekenhamer, and W. J. Padilla, "Experimental demonstration of frequency-agile terahertz metamaterials," Nat. Photonics **2**(5), 295–298 (2008).
7. H.-T. Chen, W. J. Padilla, J. M. O. Zide, A. C. Gossard, A. J. Taylor, and R. D. Averitt, "Active terahertz metamaterial devices," Nature **444**(7119), 597–600 (2006).
8. H.-T. Chen, W. J. Padilla, M. J. Cich, A. K. Azad, R. D. Averitt, and A. J. Taylor, "A metamaterial solid-state terahertz phase modulator," Nat. Photonics **3**(3), 148–151 (2009).
9. Y. Leroux, J.-C. Lacroix, C. Fave, V. Stockhausen, N. Félidj, J. Grand, A. Hohenau, and J. R. Krenn, "Active plasmonic devices with anisotropic optical response: a step toward active polarizer," Nano Lett. **9**(5), 2144–2148 (2009).
10. G. P. Wiederrecht, G. A. Wurtz, and A. Bouhelier, "Ultrafast hybrid plasmonics," Chem. Phys. Lett. **461**(4-6), 171–179 (2008).
11. N. Rotemberg, M. Betz, and H. M. Van Driel, "Ultrafast control of grating-assisted light coupling to surface plasmons," Opt. Lett. **33**, 21372139 (2008).
12. Z. Tian, A. K. Azad, X. Lu, J. Gu, J. Han, Q. Xing, A. J. Taylor, J. F. O'Hara, and W. Zhang, "Large dynamic resonance transition between surface plasmon and localized surface plasmon modes," Opt. Express **18**(12), 12482–12488 (2010).
13. M. A. Seo, H. R. Park, S. M. Koo, D. J. Park, J. H. Kang, O. K. Suwal, S. S. Choi, P. C. M. Planken, G. S. Park, N. K. Park, Q. H. Park, and D. S. Kim, "Terahertz field enhancement by a metallic nano slit operating beyond the skin-depth limit," Nat. Photonics **3**(3), 152–156 (2009).
14. B. M. Fischer, H. Helm, and P. U. Jepsen, "Chemical recognition with broadband THz spectroscopy," Proc. IEEE **95**(8), 1592–1604 (2007).
15. S. W. Koch, M. Kira, G. Khitrova, and H. M. Gibbs, "Semiconductor excitons in new light," Nat. Mater. **5**(7), 523–531 (2006).

16. J.-H. Son, "Terahertz electromagnetic interactions with biological matter and their applications," J. Appl. Phys. **105**(10), 102033 (2009).
17. C. Balaris, *Antenna Theory,* 3rd Edition, (Wiley and Sons, 2005).
18. H. Fischer, and O. J. F. Martin, "Engineering the optical response of plasmonic nanoantennas," Opt. Express **16**(12), 9144–9154 (2008).
19. V. Giannini, A. Berrier, S. A. Maier, J. A. Sánchez-Gil, and J. G. Rivas, "Scattering efficiency and near field enhancement of active semiconductor plasmonic antennas at terahertz frequencies," Opt. Express **18**(3), 2797–2807 (2010).
20. J. Gómez Rivas, J. A. Sánchez-Gil, M. Kuttge, P. Haring Bolivar, and H. Kurz, "Optically switchable mirrors for surface plasmon polaritons propagating on semiconductor surfaces," Phys. Rev. B **74**(24), 245324 (2006).
21. E. Hendry, F. J. Garcia-Vidal, L. Martin-Moreno, J. G. Rivas, M. Bonn, A. P. Hibbins, and M. J. Lockyear, "Optical control over surface-plasmon-polariton-assisted THz transmission through a slit aperture," Phys. Rev. Lett. **100**(12), 123901 (2008).
22. T. H. Isaac, W. L. Barnes, and E. Hendry, "Determining the terahertz optical properties of subwavelength films using semiconductor surface plasmons," Appl. Phys. Lett. **93**(24), 241115 (2008).
23. S. Adachi, *Handbook on physical properties of semiconductors*, Vol. 1 (Kluwer, 2004).
24. M. C. Beard, G. M. Turner, and C. A. Schmuttenmaer, "Terahertz spectroscopy," J. Phys. Chem. B **106**(29), 7146–7159 (2002).
25. D M. van Exter, and D. Grischkowsky, "Carrier dynamics of electrons and holes in moderately doped silicon," Phys. Rev. B Condens. Matter **41**(17), 12140–12149 (1990).

1. Introduction

Methods to guide and confine electromagnetic radiation in the smallest possible volume are generating new possibilities for imaging, spectroscopy and non-linear light-matter interactions beyond the diffraction limit [1]. An efficient means of achieving extreme light concentration [2,3] is to use and control localized surface plasmon polaritons (LSPPs), i.e., free charges in isolated conducting structures coherently driven by electromagnetic radiation. A myriad of fascinating phenomena originate from the interaction of electromagnetic radiation with free charges in conducting structures. In particular, LSPPs in conducting antennas are very attractive owing to their ability to focus the electromagnetic field at sub-wavelength scales leading to local field intensity enhancements of several orders of magnitude [3]. This considerable field concentration opens up novel possibilities for the exploration of non-linear optical phenomena [4,5]. Hitherto, intensive research on plasmonics is being carried out at optical and near infrared frequencies mainly involving metals [3,6–12]. However, active tuning with metals has proven challenging due to their large concentrations of charge carriers. Moreover, in the low frequency range (far-infrared, terahertz and microwaves) exciting plasmonic resonances of metallic resonators is further complicated by the lower field penetration in the metal due to the very large permittivity of metals at these frequencies [13].

In order to overcome these limitations, in this article, we demonstrate that antennas made of semiconductor can support LSPPs resonances at THz frequencies. Moreover, these resonances can be actively controlled on ultrafast time scales by optical modulation of the free charge carriers in the semiconductor. The THz regime is the range of the electromagnetic spectrum corresponding to sub-millimetre waves (1 THz corresponds to a wavelength $\lambda = 300$ μm) where many physical, chemical and biological systems have specific fingerprints [14–16]. However, technologies enabling efficient control and manipulation of THz radiation are currently limited. Therefore, the present results on the active control of LSPPs at THz frequencies are also relevant for the general effort towards filling the THz technology gap in view of useful THz applications.

The investigated structures are bowtie antennas, which are dimer structures where two triangular, conducting structures with their apex facing each other define a subwavelength gap. Bowtie antennas have been widely used at radio frequencies [17], and this geometry has recently been adopted in the field of plasmonics at visible frequencies [2,18]. Bowtie antennas strongly concentrate the field at the extremities of the individual triangular monomers, and can provide very large field enhancements [18,19]. The eigenfrequency of the collective oscillation of conduction electrons is determined by the shape and size of the antenna and by the electronic properties of its material, e.g., carrier density, effective mass and mobility. These electronic properties determine the electromagnetic impedance at the surface of the antenna. Plasmonic effects require that the penetration of the electromagnetic radiation in the

material is significant so that the incident radiation can couple efficiently to free charges. This coupling is stronger for low values of the impedance, hence permittivity, of the conductor. In this respect semiconductors are ideal candidates for active plasmonics in the THz regime: they provide not only an intrinsically better coupling of their free charges to electromagnetic fields due to their much lower permittivity compared to metals, but they also provide the possibility of tuning this permittivity in a wide range by means of the free carrier concentration that can be controlled by material doping, through thermal, optical or electrical means. Several reports are available on the propagation of surface plasmon polaritons at semiconductor surfaces [20–22], but LSPPs supported by individual semiconductor structures have not been demonstrated so far.

2. Semiconductors at Terahertz frequencies

The permittivity of doped silicon is obtained using the Drude model following the equation:

$$\varepsilon(\omega) = \varepsilon_\infty - \frac{\omega_p^2}{\omega^2 + i\gamma\omega},$$

where $\varepsilon_\infty = 11.7$, ω the angular frequency, ω_p is the angular plasma frequency, given by $\omega_p^2 = \frac{e^2 N}{\varepsilon_0 m^*}$, and γ the damping rate, $\gamma = \frac{e}{m^* \mu_n}$ with e the elementary charge, m^* the effective mass of the electrons ($m^* = 0.98 m_0$, with m_0 the electron rest mass), N the carrier concentration, and μ_n is the electron mobility. We use a carrier dependent model [23] to calculate the electron mobility in silicon.
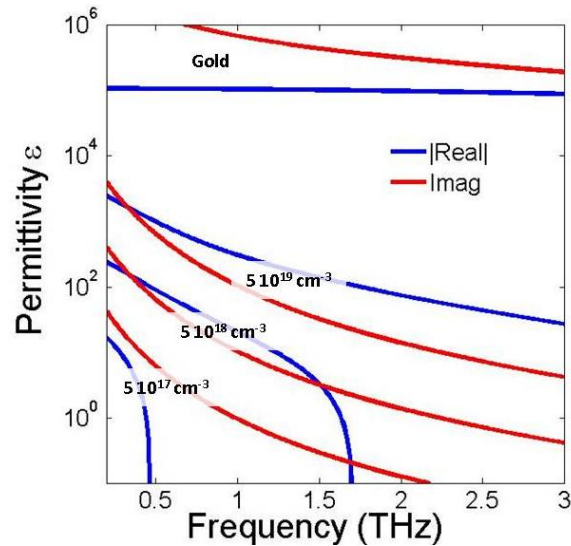

Fig. 1. Modulus of the real part and imaginary part of the permittivity of doped silicon obtained by the Drude model as a function of the frequency and of the carrier concentration. The permittivity of gold is also displayed for comparison.

Figure 1 displays the permittivity (modulus of the real part and imaginary part) of silicon as a function of the carrier concentration in a logarithmic scale. As the carrier concentration increases, the permittivity values increase and the plasma frequency shifts to higher frequencies. The plasma frequency $\nu_p = \omega_p/2\pi$ varies between 2.6 THz and 14 THz when the N varies from 1.10^{18}cm^{-3} to 3.10^{19}cm^{-3}. For sake of comparison, we have included the permittivity of gold on the same graph. The permittivity of gold is calculated using the Drude model with plasma frequency $\omega_p = 1.34.10^{16} \text{rad.s}^{-1}$, scattering rate $\gamma_p = 4.07.10^{13} \text{rad.s}^{-1}$ and

$\varepsilon_{\infty} = 1$ [13]. The permittivity of gold is three orders of magnitude higher than that of the doped silicon. Due to their large permittivities at THz frequencies, metals behave as perfect conductors, for which excitation of surface plasmon polaritons (SPPs) is not possible. Doped Si has a much lower permittivity, which facilitates the excitations of SPPs at THz frequencies. The plasmonic character of photoexcited silicon at THz frequencies was experimentally demonstrated in Ref. 13.

The skin depth of the semiconductor varies with the carrier concentration. Figure 2 illustrates the variation of the skin depth at 0.9 THz as a function of the Drude parameters: the plasma frequency and the scattering rate. The range of parameters of the silicon in the present work is indicated by a white ellipse where the skin depth varies from 40 μm to 1.7 μm. If we compare to the case of gold (orange dot on Fig. 2), we note that the skin depth of Si is much larger (several microns) than that of Au (few nanometers). Therefore the coupling of the incident radiation is much larger in the case of the silicon than in the case of a metal. For a semiconductor layer thickness of a few microns, the THz radiation penetrates completely into the material, leading to the plasmonic behavior of Si at THz frequencies.
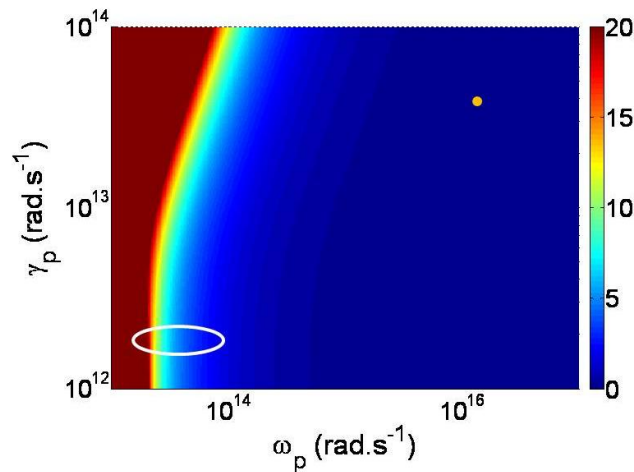

Fig. 2. Skin depth (in micrometers) as a function of the plasma frequency ω_p and of the scattering rate γ_p at the frequency of 0.9 THz. For display purposes the scale bar has been set between 0 and 20 μm. The white ellipse corresponds to the region of photoexcited silicon. The orange dot corresponds to the values for Gold.

3. Experimental

3.1 Sample fabrication

The process steps for the fabrication of the samples are as follows: a silicon-on-insulator wafer with a 1.5 μm undoped silicon top layer of given carrier concentration is bonded to a commercial amorphous quartz (fused silica) substrate of thickness 1 mm using benzocyclobutene (BCB, Dow Chemicals). The silicon top layer is not intentionally doped, unless otherwise specified. If so, the carrier doping of the silicon layer is performed by implantation of arsenic atoms. The silicon substrate and the intermediate SiO_2 layers are wet chemically etched using KOH and HF, respectively. The bowtie antennas are then patterned using conventional optical lithography and subsequent reactive ion etching step. The fabricated bowtie antennas are composed of two monomers of width 40 μm, length 100 μm and separated by a gap of 20 μm. In order to increase the signal-to-noise ratio in the THz extinction measurements shown below, instead of single antennas we have investigated samples formed by an aperiodic distribution of identical bowtie antennas with surface area coverage of 12%. An optical microscope image of a sample is shown on Fig. 3. This aperiodic distribution avoids diffraction effects in the extinction measurements. All the antennas have a

fixed orientation with all the bowtie structures parallel to each other. The antennas are placed sufficiently far away from each other to avoid near field coupling. Due to the aperiodicity, far field coupling effects average out.
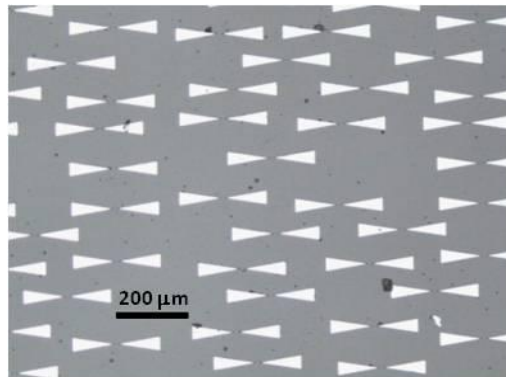

Fig. 3. Optical microscope image of the fabricated sample.

3.2 Optical pump - THz probe experiments

To investigate the excitation of LSPPs in bowtie antennas, we have measured the transmission of single-cycle, picosecond THz pulses through a sample made of bowtie antennas using time-domain THz spectroscopy [24]. This technique measures the electric field amplitude as function of time, hence providing information both on the amplitude and the phase of the electromagnetic field, and allows for picosecond time-resolution. The time-resolved THz Time-Domain Spectrometer is based on an amplified Ti:sapphire laser with 1 kHz repetition rate. The output pulses at 800 nm wavelength have a duration of 130 fs and a pulse energy of 1 mJ. Around 90% of the energy is frequency-doubled with a BBO crystal with a conversion efficiency of about 30% and used as the pump pulse to optically excite charge carriers in the sample. The area of the pump beam is about 7 mm^2. The remaining part of the output beam is split in two parts to generate and detect the THz probe pulse, respectively. The THz pulse is generated via optical rectification in a 1 mm thick ZnTe crystal. The THz field is linearly polarized. The size of the THz beam is 1.8 mm. The transmission of the THz pulse through the sample is measured by the detection pulse via electro-optic sampling in a second ZnTe crystal using a pair of balanced silicon photodetectors.
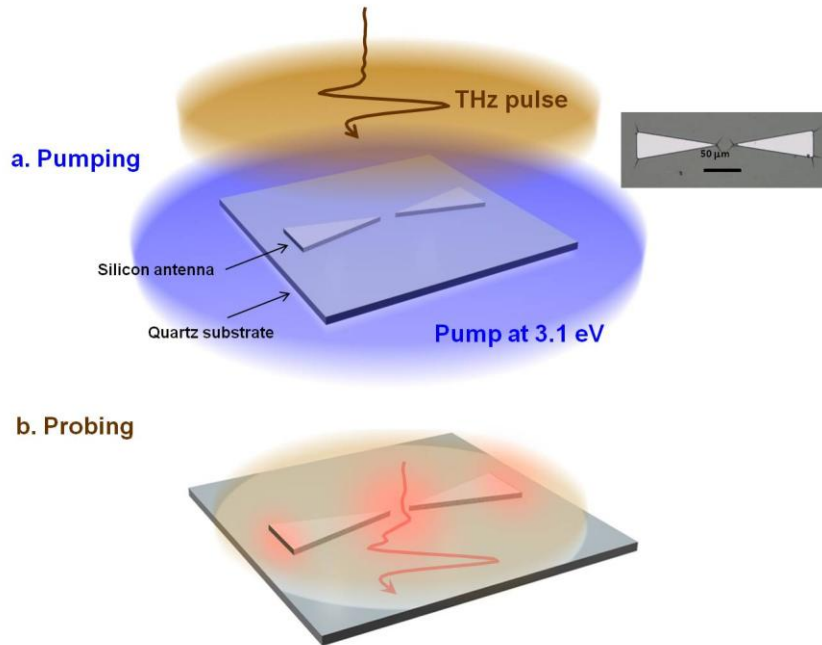
Fig. 4. Schematic drawing of the experimental configuration. (a) a resonant semiconductor bowtie antenna under optical pumping at 3.1 eV illustrated by the blue area. The THz pulse, shown as a smaller brown area, is following the pumping pulse and has a beam waist of about 1.8 mm. A typical temporal transient is shown on the THz beam. The inset is an optical microscope view of a fabricated bowtie antenna. (b) Resonant silicon antenna under THz illumination. The modified shape of the temporal THz transient is shown. The red glow indicates the regions of field enhancement around the bowtie structure.

Undoped silicon is transparent at THz frequencies. Therefore, in order to induce quasi-metallic behaviour in Si, carriers are excited above the bandgap (1.1 eV) using a ~150 femtosecond laser ('pump') pulse at a photon energy of 3.1 eV. After thermalisation and diffusion of the generated hot carriers, the response of the bowtie antenna is subsequently probed by a THz ('probe') pulse. Unless otherwise specified, the polarization of the THz beam is parallel to the long axis of the bowtie antennas. Figure 1 illustrates schematically the experimental configuration. The pump beam precedes the probe beam and creates electron-hole pairs in the bowtie antenna [Fig. 4(a)]. Then, the impinging THz radiation resonantly drives the photo-generated free electrons in the bowtie antenna and induces a THz field concentration at the base of the triangular dimers and in the gap. The loci of the field enhancements around the antenna are illustrated by transparent red areas on Fig. 4(b). The resonance of the bowtie structure induces a shape modification in the transmitted THz pulse.
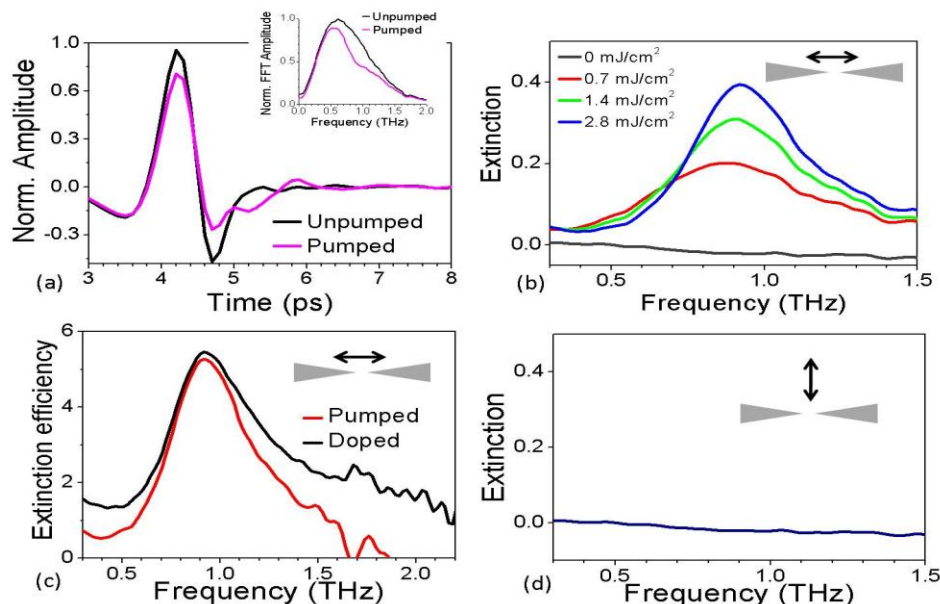
Fig. 5. (a) Temporal transients of the THz pulses after transmission through the silicon antennas in a pumped or unpumped state; the inset shows the respective FFT amplitudes; (b) Experimental extinction of a collection of silicon bowtie antennas as a function of the pumping energy. (c) Extinction efficiency of a collection of silicon bowtie antennas made of doped material compared to that of a collection of optically pumped bowtie antennas at 2.8 mJ/cm^2. The polarization of the THz radiation is parallel to the long axis of the antenna as displayed in the schematic inset; (d) Extinction of the optically pumped antenna when the polarization direction is perpendicular to the long axis of the antenna as shown on the schematic drawing in the inset.

A THz transient measured in transmission is shown on Fig. 5(a) for an unpumped sample (black curve) and a sample pumped with a pump energy of 200 μJ (magenta curve), which corresponds to a pump fluence of 2.8 mJ/cm^2. The optical pump reduces the maximum amplitude of the transmitted transient and increases the temporal dispersion of the THz pulse. Analysis of the results is most conveniently performed in the frequency domain. This analysis is done by Fourier transforming the transients to obtain the Fourier spectra [cf inset of Fig. 5(a)] and normalizing them by a reference measured through the bare substrate. Figure 5(b) displays the measured normalized amplitude extinction spectra for different pump energies. The extinction E is defined by E = 1-T, where T is the transmission amplitude. Therefore the extinction is the sum of absorption and scattering by the antennas. For unexcited silicon, no extinction peak is distinguishable. Undoped silicon acts as a dielectric and the antennas cannot support localized surface plasmon resonances. As the energy of the pump beam increases a resonant peak in the extinction spectrum develops. The optically generated free carriers are driven by the THz pulse, inducing the collective oscillation of carriers coupled to the electric field - the LSPP - which re-emits at THz frequencies, giving rise to oscillations decaying on a ~2 ps timescale. As the number of free carriers increases, the extinction peak narrows, i.e., its lifetime increases, and its strength increases. Moreover, the resonance blue-shifts at higher carrier concentrations due to the increase of the plasmon frequency. However the shift of the resonance is strongly dependent on the geometry of the antenna and the blueshift will eventually saturate.

Figure 5(c) represents the extinction efficiency of a single antenna, which is defined as the sample extinction relative to the geometrical cross-section of the illuminated antennas (red curve). The extinction is calculated here from the power spectrum of the FFT signal. The optical pump energy is 200 μJ. The excitation efficiency reaches values close to 6. One notes

here that if a material with higher mobility and lower bandgap, such as InSb, is used the performances of the antennas are expected to be improved.

Beside optical generation, the free carriers in semiconductors can be provided by material doping. Identical antennas were fabricated from n-doped Si with a doping concentration of about 4×10^{19} cm^{-3}. The extinction efficiency of the doped antennas is presented on Fig. 5(c) with the black curve. The strength and shape of the resonance of the doped antennas are comparable to that of the optically pumped ones. As can be seen on Fig. 5(d), the plasmonic resonance is not excited for THz radiation polarized perpendicular to the long axis of the antenna, This result is consistent with the antenna response dictated by the geometry of the bowties, and demonstrates that the antennas can work as polarization selective filters.

4. Finite-difference time domain simulations

In order to gain further insight into the resonant behaviour of the semiconductor bowtie antennas, we perform three-dimensional (3D) Finite Difference Time Domain (FDTD) simulations (Lumerical FDTD Solutions 6.0). The source is a total field scattered field (TFSF) source with monitors surrounding the scattering structure (silicon antenna) and perfectly matched layers (PML) surrounding the simulation area. The simulation area is taken large enough to avoid reflections at the boundaries. Two types of refining meshes are used, one surrounding the antenna and a second finer mesh comprising two parts one around the gap and the second at the edges of the antenna . The minimum size of the finer mesh is 150 nm. We simulate a bowtie antenna of triangular base 40 μm, length 100 μm, thickness 1.5 μm and gap size of 20 μm. The calculation is performed over one fourth of the structure, taking advantage of the symmetry axes of the antenna structure. The simulated antennas are placed on top of a substrate of refractive index 2 in a background environment of refractive index 1. The permittivity of silicon is obtained from a plasma model based on the Drude model, as described in section 2.
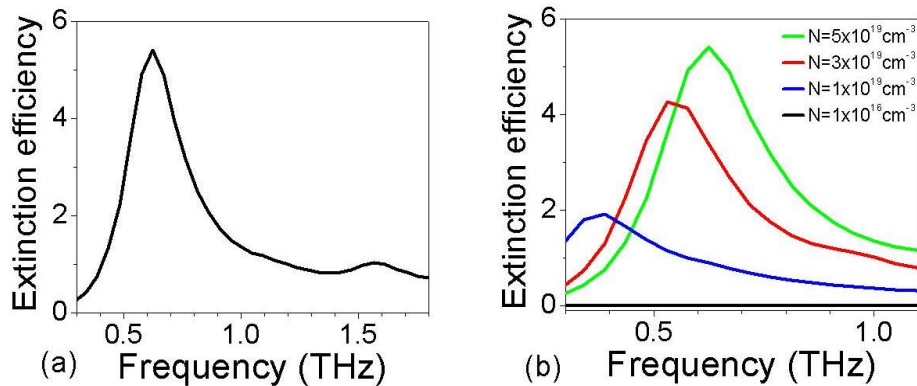
Fig. 6. Extinction efficiencies obtained by three dimensional finite-difference time-domain simulations of silicon bowtie antennas. The permittivity is obtained by the Drude model. (a) Extinction efficiency for a silicon bowtie antenna of width 40 μm, length 100 μm, and gap 20 μm. The carrier concentration is 5×10^{19} cm^{-3}. (b) Extinction efficiency as a function of the carrier concentration.

Figure 6 displays the result of the modelling of the antenna response. A comparison of Fig. 6(a) (FDTD) with Fig. 5(c) (experiment) indicates a qualitative agreement in both extinction efficiency and shape of the resonances. Figure 6(b) shows the behaviour of the simulated structure with increasing carrier concentration: the resonances both increase in strength and shift to higher frequencies with doping. However, the magnitude of the shift is smaller in the experimental data. Discrepancies in the resonance shape and frequency can be explained by differences in the geometry of the fabricated and simulated antennas, such as differences in the slope of the etched sidewalls and shape of the apex. Moreover, the behaviour of the carriers in the semiconductor may differ from the Drude model by a modified

damping rate due to variations in the carrier collision time, inter/intravalley phonon scattering and scattering with ionized impurities [25]. The differences in damping rate may explain discrepancies in the magnitude of the blue shift and linewidth of the resonances between experiments and simulations since an increase of the scattering rate in the simulations blue-shifts the resonance and increases the resonance linewidth (not shown).

5. Ultrafast switching of the antenna resonances

One of the unique properties of semiconductor antennas is that they allow for ultrafast optical switching of LSPPs. By varying the time delay between the optical pump and the THz probe, we can determine the response time of the LSPPs to the optical pump. The time-resolved differential THz signal between pumped and unpumped state of the silicon antennas is obtained as the difference signal when the path of the pump is alternatively free or blocked by a chopper. The optical pump arrives at t = 0 ps. When the THz pulse arrives before the pump, there is no difference in the THz absorption between the two paths since no photo-carriers are generated. However, when the THz pulse arrives after the pump, the THz signal couples to the generated free carriers and the difference THz signal increases.
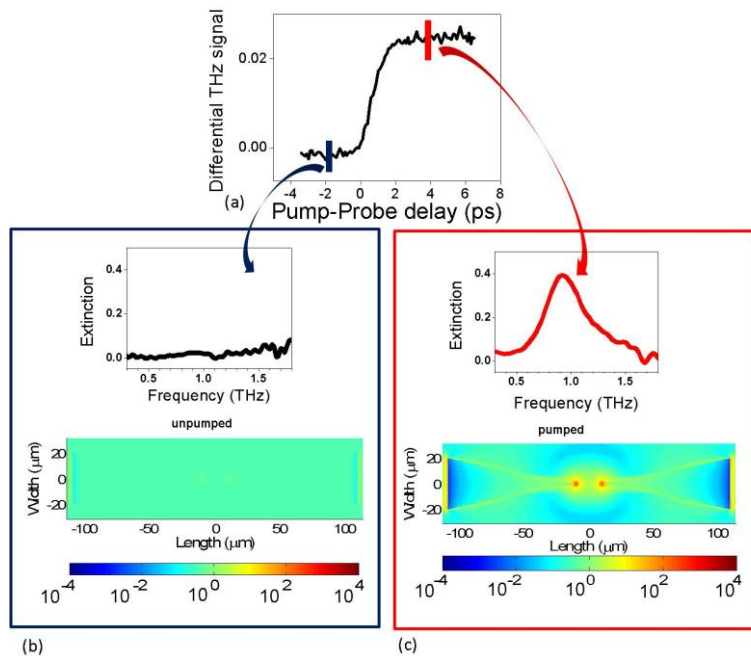

Fig. 7. (a) Time resolved differential signal pump ON/pump OFF as a function of the pump-probe delay; (b) Extinction cross-section measured before the arrival of the pump pulse (top) and simulation of the field intensity enhancement profile around the bowtie antenna before the arrival of the pump pulse (bottom). The field intensity enhancement is displayed in logarithmic scale; (c) Extinction cross-section measured after the arrival of the pump pulse (top) and simulation of the field intensity profile around the bowtie antenna after the arrival of the pump pulse (bottom). The field intensity enhancement is displayed in logarithmic scale.

Figure 7(a) shows the time dependence of the differential THz signal. The ~2 ps rise time of the signal can be attributed to thermalisation and diffusion of charge carriers after photo-excitation. After this time, the differential THz signal is constant in the range of times displayed in Fig. 7, and will decrease slowly due to the long bulk carrier lifetime (typically 500 ns) as well as non-radiative recombination at the silicon/air interfaces and etched sidewalls. In direct bandgap semiconductors, recombination is faster owing to radiative processes and typically happens within a few ns or less. Non-radiative recombination can be

increased by surface treatment or by increasing the number of defect states and deep recombination centers in the bulk material.

Inherently linked to the behaviour of the resonance in the far field (as measured with extinction efficiencies), the near-field intensity can be enhanced on ultrafast time scales (few ps) as shown in Fig. 7. Figure 7(b) and 7(c) display the electric field intensity enhancement, in a horizontal cross section of the antennas at their middle height, of the antenna in the OFF (b) and ON (c) states as calculated by 3D FDTD. Before the arrival of the pump pulse (OFF state), the field enhancement is very low and almost constant at 1. After the arrival of the pump pulse, the increase in field intensity enhancement is up to a factor of 10^4 at the tip of the antennas. The field is mainly squeezed in the gap of the antennas into an area of about 1600 μm^3. This represents a field concentration of about 10^5 times compared to λ^3 where λ is the wavelength of the THz radiation. We note that although extreme field enhancement can be locally achieved in the gap of the bowtie antenna, the overall field enhancement is in accordance with the Q factor of the resonances.

7. Conclusion

In summary, this article proposes the use of semiconductors for the excitation of localized surface plasmon polaritons at THz frequencies. By means of bowtie antennas made of silicon, ultrafast control of the resonances over a range of extinction efficiencies up to 6 is achieved within few picoseconds. The experimental demonstration of the excitability and ultrafast active control of plasmonic resonances of silicon antennas at THz frequencies paves the way towards a wide range of novel fundamental and applied research in sensing, spectroscopy, and non-linear interactions.

Acknowledgments